

See discussions, stats, and author profiles for this publication at: <https://www.researchgate.net/publication/231649556>

# Efficient Photoinduced Charge Injection from Chemical Bath Deposited CdS into Mesoporous TiO<sub>2</sub> Probed with Time-Resolved Microwave Conductivity

ARTICLE in THE JOURNAL OF PHYSICAL CHEMISTRY C · APRIL 2008

Impact Factor: 4.77 · DOI: 10.1021/jp800527r

CITATIONS

27

READS

21

7 AUTHORS, INCLUDING:



Jorge Piris

European Space Agency

31 PUBLICATIONS 2,108 CITATIONS

SEE PROFILE



Andrew G Norman

National Renewable Energy Laboratory

203 PUBLICATIONS 2,685 CITATIONS

SEE PROFILE



Garry Rumbles

National Renewable Energy Laboratory

208 PUBLICATIONS 6,308 CITATIONS

SEE PROFILE



Nikos Kopidakis

National Renewable Energy Laboratory, G...

117 PUBLICATIONS 5,424 CITATIONS

SEE PROFILE

# Efficient Photoinduced Charge Injection from Chemical Bath Deposited CdS into Mesoporous TiO<sub>2</sub> Probed with Time-Resolved Microwave Conductivity

Jorge Piris,<sup>†</sup> Andrew J. Ferguson, Jeff L. Blackburn, Andrew G. Norman, Garry Rumbles, Don C. Selmarten, and Nikos Kopidakis\*

National Renewable Energy Laboratory, 1617 Cole Boulevard, Golden, Colorado 80401

Received: January 18, 2008; Revised Manuscript Received: March 5, 2008

We use the contactless time-resolved microwave conductivity (TRMC) technique to investigate the photoconductance of CdS-coated mesoporous TiO<sub>2</sub> and ZrO<sub>2</sub>. The CdS domains were grown directly on the surface of the oxide by a chemical bath deposition method. Mobile charge carriers are generated with a low yield following photoexcitation of CdS grown on ZrO<sub>2</sub>; there is no injection into the oxide and the short-lived photoconductance signal is attributed to the hole in CdS. In contrast, illumination of CdS domains grown on TiO<sub>2</sub> results in very efficient electron injection into the TiO<sub>2</sub> nanoparticles, producing long-lived charge carriers. We show that the quantum yield for electron injection into TiO<sub>2</sub> per photon absorbed by the CdS sensitizer is close to unity. The photoconductance action spectrum follows the absorption of the CdS domains, which indicates that the charge injection efficiency does not depend on wavelength in the range where the CdS absorbs (425–550 nm).

## 1. Introduction

Mesoporous TiO<sub>2</sub> offers a robust template for the assembly and testing of sensitizers for solar energy conversion applications. Quantum-confined inorganic semiconductor sensitizers are attractive because of their size-dependent properties that allow tuning of the absorption spectrum and energetics of the sensitizer–oxide system. In particular, CdS and CdSe can relatively easily be deposited onto TiO<sub>2</sub> with chemical bath techniques<sup>1–7</sup> or linked as nanoparticles to the oxide with bifunctional linker molecules.<sup>8,9</sup> Electron injection from the photoexcited sensitizer into TiO<sub>2</sub> is the primary step in the photocurrent generation process and is typically studied by optical probe techniques such as steady-state and transient photoluminescence<sup>7,10</sup> and transient absorption.<sup>7–9</sup> These techniques provide compelling qualitative evidence for charge injection from the photoexcited CdS sensitizer to TiO<sub>2</sub> and a quantitative measure of the related characteristic times or charge-transfer rate constants.

The photoconductivity of complete photovoltaic devices based on CdS-sensitized TiO<sub>2</sub> has been reported.<sup>1–6,9</sup> In these reports, sensitization is demonstrated by the shift of the photoconductivity action spectrum toward visible wavelengths compared to the bare (unsensitized) oxide. Measurements of the incident photon to current conversion efficiency (IPCE) give the yield of electrons extracted from the device per photon incident on the sample, which provides a lower limit for the quantum yield for photoinduced electron injection from the sensitizer to the oxide.<sup>11</sup>

In a previous report we presented photoluminescence spectroscopy and transient absorption measurements on CdS domains grown onto mesoporous TiO<sub>2</sub> and ZrO<sub>2</sub> by successive ionic layer adsorption and reaction (SILAR).<sup>7</sup> Steady-state photolumines-

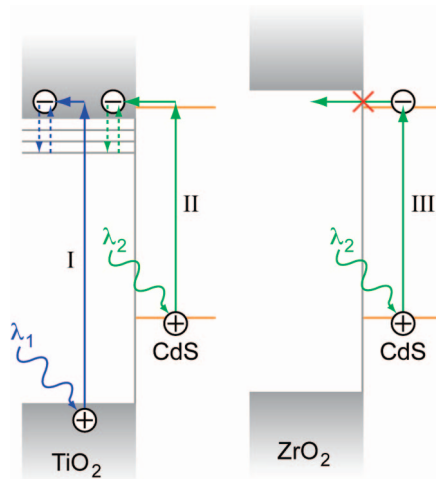


**Figure 1.** The different photoexcitation schemes presented in this paper. Direct band gap photoexcitation of TiO<sub>2</sub> (with and without CdS sensitizer) is shown by process I ( $\lambda_1 = 300$  nm). Photoexcitation of the CdS sensitizer on TiO<sub>2</sub> in the visible is shown by process II ( $\lambda_2 = 425$ –550 nm). The vertical dotted arrows in processes I and II represent the trapping and detrapping of electrons in TiO<sub>2</sub>. Process III represents photoexcitation of the CdS sensitizer on ZrO<sub>2</sub>, where electron injection to the oxide does not occur.

cence (PL) spectroscopy showed a strong PL signal when CdS was deposited on ZrO<sub>2</sub>, and that the PL was quenched when CdS was deposited on TiO<sub>2</sub>. This observation indicates that, when deposited on zirconia, CdS forms isolated domains that do not communicate electronically with each other or with the underlying oxide. When CdS is grown onto TiO<sub>2</sub>, electronic communication between CdS and the oxide becomes possible, due to the higher electron affinity of TiO<sub>2</sub>. The underlying assumption that CdS, grown by SILAR, has the same structure on zirconia and titania is substantiated by the similar surface chemistry of the two oxides. The scheme shown in Figure 1 summarizes the results from that work and sets the stage for the studies presented here. Transient absorption (TA) measure-

\* To whom correspondence should be addressed. E-mail: nikos\_kopidakis@nrel.gov.

<sup>†</sup> Current address: Opto-electronic Materials, DelftChemTech, Faculty of Applied Sciences, Delft University of Technology, Julianalaan 136, 2628 BL Delft, The Netherlands.

ments probing the time evolution of the population of the photoexcited state of CdS showed that charge injection from CdS to TiO<sub>2</sub> (through process II of Figure 1) occurs in time scales ca. 10–50 ps.<sup>7</sup> In contrast, photoinduced charge injection to ZrO<sub>2</sub> does not occur (process III of Figure 1), in which case the excited state of CdS has a lifetime exceeding 80 ps.<sup>7</sup>

In this work we present direct photoconductance measurements of the TiO<sub>2</sub>/CdS composite and focus on electron injection from the CdS sensitizer to the oxide, which is the primary step in photocurrent generation in a complete photovoltaic device. To isolate the sensitizer/oxide system and study it with no additional components (e.g., hole-transporting media in the pores of the oxide), we use the contactless time-resolved microwave conductivity (TRMC) technique,<sup>12</sup> which is based on exciting the sample with a laser pulse and probing the photoconductance with a microwave beam. The technique allows us to investigate carrier generation efficiencies, carrier mobilities, trapping processes, and the lifetime of free carriers. We use ultraviolet excitation to primarily excite the oxide (direct band gap excitation, process I in Figure 1) and produce an electron and a hole in TiO<sub>2</sub>. Tuning the excitation wavelength toward the visible, where the oxide is transparent, we can excite the CdS nanocrystals on the surface (processes II and III in Figure 1) and investigate electron injection to the oxide. Our measurements confirm that charge injection from CdS to TiO<sub>2</sub> occurs (process II in Figure 1), but does not take place from CdS to ZrO<sub>2</sub> (process III in Figure 1). We also investigate the trapping of electrons generated or injected in TiO<sub>2</sub>, shown by the vertical dotted arrows in processes I and II, and show that the CdS nanocrystals do not change surface trapping of electrons in TiO<sub>2</sub>. The high-frequency ac probe allows us to measure the hole mobility in the confined CdS domains, which is found to be higher than the electron mobility in the TiO<sub>2</sub> nanoparticles. The latter observation distinguishes the present study from previous work on sensitizing TiO<sub>2</sub> with organic sensitizers and probing free carrier generation with microwaves.<sup>13–21</sup> In those studies the carrier mobility in the organic sensitizer was much lower than the electron mobility in TiO<sub>2</sub> and microwave absorption was dominated by electrons in TiO<sub>2</sub>, making it possible to directly quantify the efficiency of charge injection from the sensitizer. In the present work the microwave absorption signal is more complicated and a deconvolution procedure is needed to quantify the efficiency of charge injection to TiO<sub>2</sub> per photon absorbed in CdS. As we will show, this efficiency is very close to 100% for the TiO<sub>2</sub>/CdS system presented here, and the efficiency does not change with wavelength in the range where the sensitizer absorbs.

## 2. Materials and Methods

**2.1. Sample Preparation.** The TiO<sub>2</sub> and ZrO<sub>2</sub> colloids with average particle size of ca. 20 nm were synthesized as described elsewhere.<sup>7</sup> The resulting colloidal suspension was mixed with poly(ethylene glycol) to form a slurry, which was doctor bladed onto a 25 × 11 × 1 mm quartz substrate and sintered at 450 °C for 1 h. After performing microwave photoconductance measurements of the bare layers, the nanoparticle films were then exposed to the successive ionic layer adsorption and reaction (SILAR) process to grow the CdS sensitizer, as reported previously.<sup>2,3,7</sup> In brief, the oxide film is dipped for 2 min into a saturated cadmium acetate solution, rinsed with deionized water, then dipped for 2 min into a 0.1 M Na<sub>2</sub>S solution, and rinsed again. For the samples presented here this reaction cycle was repeated eight times. With this process, nanocrystalline CdS domains are grown as disklike domains directly on the surface

of the oxide throughout the entire thickness of the porous film. The thickness of the films used in this work was between 2 and 4 μm.

**2.2. Transmission Electron Microscopy (TEM) Imaging.** TEM characterization was carried out on a Philips CM30 TEM operated at 300 kV. Lattice images were acquired with an objective aperture that admitted contributions from low-index reflections. The samples were prepared in the following manner. Eight cycles of CdS deposition were carried out on a TiO<sub>2</sub> film on a glass substrate. After deposition, the film was scraped off the glass substrate into a vial. Approximately 0.5 mL of toluene was added to the vial, and this suspension was sonicated for several minutes in a bath sonicator. Approximately 4 μL of the sonicated suspension was micropipetted onto a carbon-coated Cu grid for TEM analysis.

**2.3. Optical Absorption and Microwave Photoconductance Measurements.** The fraction of incident light transmitted,  $F_T$ , and reflected,  $F_R$ , by each sample was measured with a Cary 500 spectrophotometer fitted with an integrating sphere. The fraction,  $F_A$ , of incident photons actually absorbed within the sample, usually called the attenuation spectrum, was calculated as

$$F_A = 1 - (F_T + F_R) \quad (1)$$

The photoconductance of the films was measured using the flash-photolysis time-resolved microwave conductivity (FP-TRMC) technique as described previously by Warman and co-workers.<sup>12</sup> The experimental setup is similar to that described elsewhere.<sup>18</sup> For photoexcitation in the visible, the third harmonic at 355 nm of a Q-switched Nd:YAG laser (Surelite, Continuum) was used to pump an optical parametric oscillator (OPO) (Panther, Continuum), yielding 5 ns pulses tunable in the range 420–700 nm. To obtain pulses in the UV, the output of the OPO was frequency-doubled by a second harmonic generator. The output beam was directed and expanded using fused silica prisms and lenses. A set of neutral density filters was used to attenuate the beam and vary its intensity over 4 orders of magnitude. The pulse energy was continuously monitored by directing a small portion of the beam (ca. 10%) onto a pyroelectric sensor.

The samples were mounted inside a resonant cavity at the end of an X-band microwave waveguide. One end of the cavity was closed with a grating end plate, through which the samples were photoexcited. The grating is an almost perfect mirror for the TE<sub>10</sub> mode microwaves that propagate in the waveguides. The other end of the cavity was closed with an iris plate that partially reflects the microwaves. The frequency of the microwaves (typically around 9 GHz) is tuned so that the sample is at the position of the maximum electric field of the standing wave pattern. Because of the creation of oxygen vacancies in TiO<sub>2</sub> at low oxygen partial pressure,<sup>22</sup> measurements were performed in air. An electron scavenging mixture of 10% of SF<sub>6</sub> in N<sub>2</sub> at 1 atm of pressure was used to test for the presence of photoemitted electrons from the surface of the film, which was found to be negligible for these samples.<sup>23</sup>

The microwaves were generated by a Gunn diode (Midcentury MC16/34B) mounted in a resonant cavity. The resonant frequency could be adjusted between 8.4 and 11 GHz by changing the inner dimensions of the cavity with a plunger. The output power was directed into the cell by a circulator. The remaining power not absorbed by the sample was reflected and directed by the circulator to the detector (IN23 Schottky barrier diode). The output voltage of the diode is amplified with a 1.1 GHz amplifier (Femto HSA-X-1-40) and recorded with a

digital oscilloscope (TDS1234, Tektronix). To minimize electromagnetic pickup, the microwave source, power supply, detector, and amplifier were enclosed in a Faraday cage.

**2.4. Photoconductance Data Analysis.** Transient changes in the conductance of the sample upon illumination with short laser pulses were monitored with nanosecond time resolution as variations in the microwave power,  $\Delta P$ . The relative change in microwave power can be directly related to the photoinduced conductance,  $\Delta G$ , of the films by

$$\frac{\Delta P}{P} = -K\Delta G \quad (2)$$

where  $K$  is an experimentally determined calibration factor derived from the resonance characteristics of the cavity and the dielectric properties of the samples used.<sup>24</sup> Since charge carriers are generated during the pulse and eventually decay,  $\Delta G$  is time dependent and is referred to as the “photoconductance transient”,  $\Delta G(t)$ .

The peak, or end-of-pulse (EOP), value of the conductance can be related to the sum of the mobilities of charge carriers (electrons and holes),  $\Sigma\mu$ , by<sup>18</sup>

$$\Delta G_{\text{EOP}} = I_0 F_A \beta q_e \left[ \phi \Sigma\mu \right]_{\text{EOP}} \quad (3)$$

with a dimensionless parameter  $\phi$  discussed in more detail below. In eq 3,  $I_0$  is the incident photon flux,  $F_A$  is the fraction of incident light absorbed by the film,  $\beta$  is a dimensionless geometric parameter of the waveguide (on the order of 2 for the X-band waveguide used here), and  $q_e$  is the elementary charge.

Assuming no recombination during the pulse, the parameter  $\phi$  represents the quantum yield for free carrier generation per photon absorbed.<sup>18,20</sup> Conversely, if significant decay occurs within the duration of the pulse, the values of  $\phi$  calculated from eq 3 will be a lower limit to the yield. In general,  $\phi$  signifies the yield for free carrier generation that we measure at the peak of the photoconductivity with the TRMC technique.

In the absence of an independent measurement of the mobility of free carriers at microwave frequencies, it is not possible to separate the yield and the mobility in eq 3. As will be discussed below, with appropriate comparisons between samples, one can still draw conclusions regarding the values of the yield or the mobility separately.

The data in this paper are presented in one of three forms: (1) Time-dependent data are presented as the absorbed-intensity-normalized photoconductance, given by  $\Delta G(t)/(I_0 F_A \beta q_e)$ , so that the peak value corresponds to the EOP value of  $\phi \Sigma\mu$ , (2) the  $\phi \Sigma\mu$  product at EOP is used to show the light-intensity-dependence data, and (3) the photoconductance action spectrum is presented as the incident-intensity-normalized photoconductance, given by  $\Delta G_{\text{EOP}}/(I_0 \beta q_e)$ .

### 3. Results

**3.1. TEM Imaging.** High-resolution TEM images of CdS domains on TiO<sub>2</sub> nanoparticles, grown with eight reaction cycles, are shown in Figure 2. The CdS domains were identified by measuring the lattice plane spacing, which was in very close agreement with that expected for wurtzite CdS. The domains grow as disks onto the TiO<sub>2</sub> nanoparticles and for eight reaction cycles their average dimensions are ca. 15 nm in diameter and 5 nm in thickness.

**3.2. Absorption Spectra.** The optical attenuation spectra of the samples studied are shown in Figure 3. The contribution of the CdS nanocrystals was estimated by subtracting the spectra measured for bare ZrO<sub>2</sub> from the same sample after the SILAR

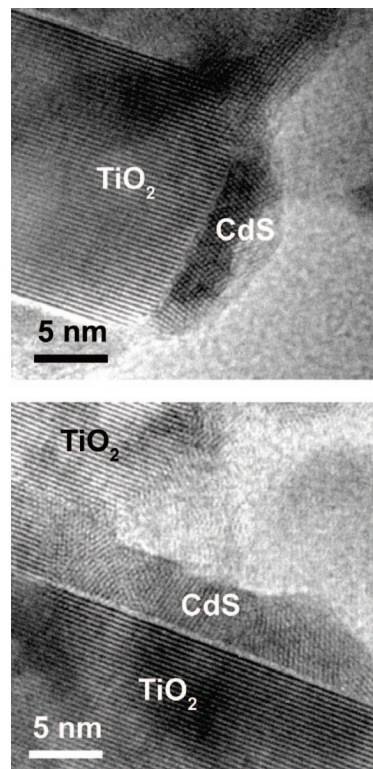


**Figure 2.** High-resolution TEM images of CdS domains grown by SILAR (eight reaction cycles) onto a TiO<sub>2</sub> nanoparticle film.

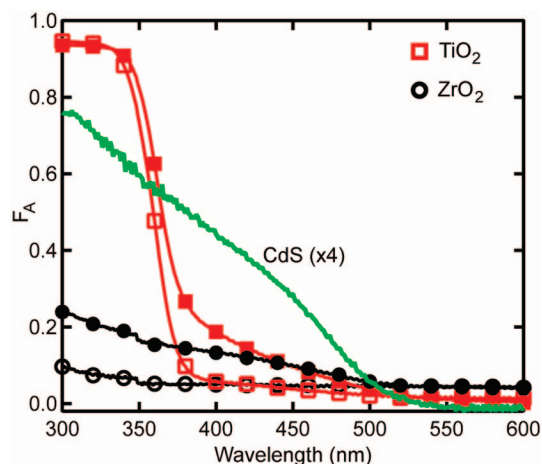


**Figure 3.** Attenuation spectra,  $F_A$ , of the samples studied. Squares indicate samples based on TiO<sub>2</sub> and circles indicate samples based on ZrO<sub>2</sub>; empty symbols denote the bare oxide and filled symbols denote the oxide coated with CdS domains. Also shown with a green line is the difference between the spectra measured for the ZrO<sub>2</sub> sample before and after CdS deposition. The CdS domains were grown with eight reaction cycles.

process, and is also shown. The CdS domains extend the absorbance of the TiO<sub>2</sub> and ZrO<sub>2</sub> samples from their onsets in the UV well into the visible. The broad absorption reflects the wide distribution of the CdS domain sizes. The onset of absorption from CdS in Figure 3 is ca. 510 nm, corresponding to an energy of 2.43 eV, which is close to the 2.5 eV band gap of bulk CdS. Indeed at eight reaction cycles the CdS domains approach their bulk absorption behavior.<sup>7</sup>

**3.3. Photoconductance Measurements.** Photoconductance transients measured under similar photon fluxes for TiO<sub>2</sub> and TiO<sub>2</sub>/CdS are shown in Figure 4. A transient from the ZrO<sub>2</sub>/CdS sample excited at 425 nm is also shown for comparison.



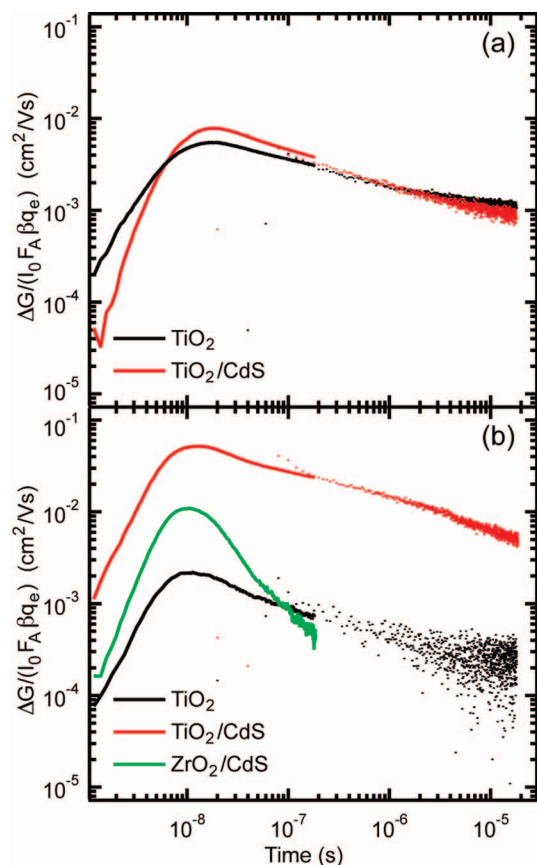


**Figure 4.** Absorbed-intensity-normalized photoconductance transients: (a) 300 nm excitation of bare TiO<sub>2</sub> (black) and CdS-sensitized TiO<sub>2</sub> (red), and (b) 425 nm excitation of bare TiO<sub>2</sub> (black), CdS-sensitized TiO<sub>2</sub> (red), and CdS-coated ZrO<sub>2</sub> (green). All transients were measured at similar incident photon fluences of  $I_0 \approx 5 \times 10^{14} \text{ cm}^{-2}$ . Each trace shown is composed of two measurements: one for short times (<200 ns) depicted with a line and one for long times (200 ns–20 μs) depicted with dots.

The observation of a photoconductance transient from the CdS/ZrO<sub>2</sub> is remarkable and indicates the photogeneration of free carriers in isolated CdS domains even when charge injection to the oxide does not occur.

Photoconductance transients obtained upon irradiation at 425 nm of the ZrO<sub>2</sub> and ZrO<sub>2</sub>/CdS samples are shown in Figure 5. The transient from the CdS/ZrO<sub>2</sub> sample decays rapidly to the signal from bare ZrO<sub>2</sub> with a characteristic time comparable to the response time of the microwave cavity. As will be discussed below, this signal is attributed to photogenerated holes in CdS.

Despite the lack of absorbance at 425 nm, a very low signal is obtained for the bare ZrO<sub>2</sub> sample. This is attributed to sub-band-gap excitation and formation of mobile charge carriers, which is still detectable by TRMC despite the relatively low efficiency of this process.

The end-of-pulse values of  $\varphi \Sigma \mu$  (calculated using eq 3) under direct band gap photoexcitation at 300 nm and excitation with 425 nm pulses are shown in Figure 6. Under excitation at 425 nm at low light intensities, the CdS-sensitized TiO<sub>2</sub> sample shows a  $\varphi \Sigma \mu$  product that is a factor of 3 higher than that of the CdS/ZrO<sub>2</sub> sample. Also,  $\varphi \Sigma \mu$  for the CdS/TiO<sub>2</sub> sample at low intensities reaches a plateau around  $0.1 \text{ cm}^2/\text{Vs}$ , which is higher than that of bare TiO<sub>2</sub> under 300 nm excitation, and has a different light intensity dependence. As we will discuss in detail below, this observation is consistent with the end-of-pulse signal for the CdS/TiO<sub>2</sub> sample being dominated by holes left in CdS after electron injection to TiO<sub>2</sub>. Below we will show

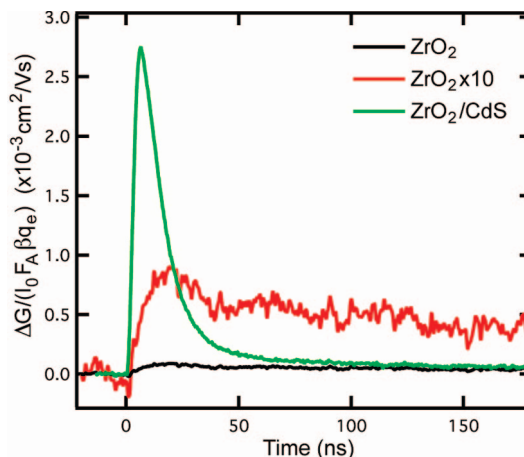


**Figure 5.** Absorbed-intensity-normalized photoconductance transients obtained upon irradiation of CdS-coated ZrO<sub>2</sub> (green line) and bare ZrO<sub>2</sub> (black line) with 425 nm laser pulses. The incident photon flux,  $I_0$ , was  $5 \times 10^{15} \text{ cm}^{-2}$ .

how the two contributions to  $\varphi \Sigma \mu$  (holes in CdS at early times and electrons in TiO<sub>2</sub> at longer time) can be extracted from the signal to elucidate the yield for electron injection to TiO<sub>2</sub> after photoexcitation of CdS.

The photoconductance action spectrum for the CdS-sensitized TiO<sub>2</sub> sample between 425 and 550 nm is shown in Figure 7. The attenuation spectrum of the sample is also shown for comparison.

#### 4. Discussion

The data obtained for the bare TiO<sub>2</sub> layer under 300 nm illumination, as shown in Figure 6a, are in very good agreement with previous work.<sup>18</sup> Due to the high dielectric constant of TiO<sub>2</sub>, the quantum yield for free carrier generation per photon absorbed of energy higher than the band gap is generally assumed to be close to 1, and therefore the  $\varphi \Sigma \mu$  product would essentially be equal to the electron mobility,  $\mu_{e,\text{TiO}_2}$ , in TiO<sub>2</sub>.<sup>18</sup> This is certainly the case for chemical vapor deposited and polycrystalline material, but for a sol-gel prepared nanocrystalline material surface trapping and electron–electron interactions limit the  $\varphi \Sigma \mu$  product at low excitation intensities.<sup>18,24</sup> The rise of the signal at low light intensities has been attributed to trap filling in TiO<sub>2</sub>,<sup>18,25–31</sup> depicted by the electron trapping and detrapping processes, illustrated by the vertical dotted arrows in process I of Figure 1. The subsequent decrease at high light intensities follows an inverse square-root dependence on light intensity (Figure 6a) and has been attributed to electron–electron interactions when the excitation level exceeds one photogenerated electron per particle.<sup>18</sup> The fact that the data shown in Figure 6a do not reach a plateau indicates that both processes overlap, limiting the  $\varphi \Sigma \mu$  product at all measured light intensities. This provides further support for  $\varphi \Sigma \mu$  being a lower limit for the trap-free mobility of electrons in TiO<sub>2</sub>. It is interesting to note that the data shown here overlap for all light intensities almost perfectly with previous results;<sup>18</sup> in that study bias illumination of the sample suppressed the trap-filling regime and the trap-free mobility of electrons was estimated to be  $0.034 \text{ cm}^2/\text{Vs}$ , in very good agreement with the maximum value,  $0.03 \text{ cm}^2/\text{Vs}$  shown in Figure 6a.

Exciting the CdS-sensitized TiO<sub>2</sub> with 300 nm pulses gives a  $\varphi \Sigma \mu$  product very slightly higher than that of the bare TiO<sub>2</sub>. At this wavelength the light is primarily absorbed by the TiO<sub>2</sub> in both samples and generates electron–hole pairs in the TiO<sub>2</sub>

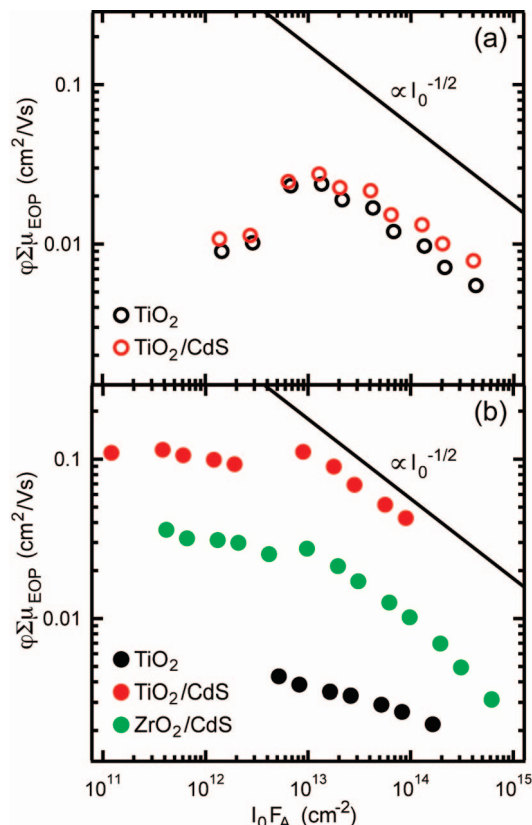


**Figure 6.** The  $\varphi \Sigma \mu$  product for (a) bare TiO<sub>2</sub> (black) and CdS-sensitized TiO<sub>2</sub> (red) under 300 nm illumination and (b) bare TiO<sub>2</sub> (black), CdS-sensitized TiO<sub>2</sub> (red), and CdS-coated ZrO<sub>2</sub> (green) photoexcited with 425 nm pulses. Note that the scales are the same in both panels. The line indicates an inverse square-root dependence on incident light intensity.

nanoparticles, according to process I of Figure 1. The trap-filling regime for electrons in TiO<sub>2</sub> at low light intensities is essentially unaltered by the presence of the CdS domains. This observation is remarkable considering recent evidence for the location of electron traps on the surface of TiO<sub>2</sub> nanoparticles in dye-sensitized, electrolyte-filled samples.<sup>25,26</sup> In the present case, CdS deposited with eight reaction cycles only partially covers the TiO<sub>2</sub> surface, and thus it is plausible that the exposed TiO<sub>2</sub> surface still appears to dominate the trapping of electrons.

The similar magnitude of the two data sets in Figure 6a indicates that under 300 nm excitation the photoconductance of the CdS-sensitized TiO<sub>2</sub> sample is also dominated by the oxide and charge injection from TiO<sub>2</sub> into CdS does not effectively occur. The small increase observed in the  $\varphi \Sigma \mu$  product of the CdS-sensitized sample is attributed to the contribution of photoexcited CdS which occurs, despite almost complete attenuation of the light at 300 nm by the TiO<sub>2</sub>, because photocarriers in CdS have high mobility, as will be discussed below.

The signal from the bare TiO<sub>2</sub> sample illuminated at 425 nm is attributed to sub-band-gap excitation and formation of mobile charge carriers within the nanoparticles.<sup>18</sup> Since the electron is much more mobile than the hole in anatase TiO<sub>2</sub>, the signal is dominated by the electrons.<sup>18</sup> At 425 nm, as shown in Figure 4b, the signal from the CdS-sensitized TiO<sub>2</sub> sample is more than an order of magnitude higher and much longer lived than the signal for the ZrO<sub>2</sub>/CdS system excited at the same wavelength. This is direct evidence for efficient electron injection occurring from the excited CdS domains into the

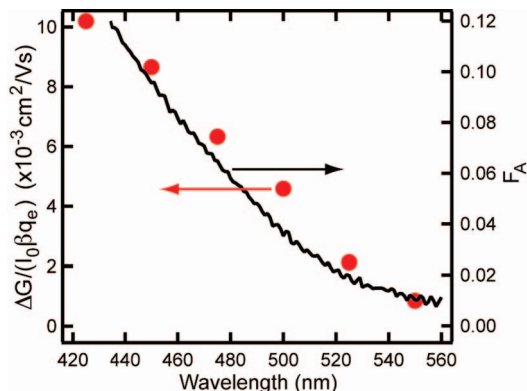


**Figure 7.** Photoconductance action spectrum for CdS-sensitized TiO<sub>2</sub>. The left axis corresponds to the incident-intensity-normalized photoconductance values (filled circles) obtained at excitation densities of ca. 10<sup>13</sup> photons/cm<sup>2</sup>/pulse. The right axis corresponds to the optical attenuation spectrum (solid line).

conduction band of TiO<sub>2</sub> (process II of Figure 1), as will be discussed below.

In the case of CdS-coated ZrO<sub>2</sub>, the photoconductance is enhanced compared to that of bare ZrO<sub>2</sub>, indicating that mobile charge carriers are generated upon photoexcitation of the CdS domains (process III in Figure 1), but the very short lifetimes indicate that charge injection to the oxide does not occur, in agreement with previous work.<sup>7</sup> If charge transfer did occur from CdS to ZrO<sub>2</sub>, electrons injected in the conduction band of the ZrO<sub>2</sub> would be efficiently shielded from the holes left in CdS by the high dielectric constant of the oxide and would diffuse away from the interface. This process would result in retardation of interfacial recombination, resulting in much longer carrier decay times, as is observed in the CdS-sensitized TiO<sub>2</sub> sample here. Similar behavior has been observed in previous studies of smooth TiO<sub>2</sub> sensitized with organic molecules and polymers.<sup>13–17,19–21</sup> Therefore, in the present work, CdS domains grown onto ZrO<sub>2</sub> can effectively be treated as isolated CdS islands on an inert mesoporous oxide.

The size dependence of the electronic properties of the CdS domains are influenced by the interaction of the excited electrons with their boundaries. In the case of crystals with a large aspect ratio, as in the present case, quantum confinement effects may manifest themselves as a result of confinement in only one direction, while bulk-like transport may still be possible in the other directions. The reported bulk mobilities in CdS are 350 cm<sup>2</sup>/V s for electrons and 40 cm<sup>2</sup>/V s for holes.<sup>32</sup> Using these values, it is possible to estimate the field-induced displacement during a half-cycle of the microwave probe field using  $\delta d = \mu E(\delta t)$ , where  $\mu$  is the mobility,  $E$  is the electric field of the microwaves, and  $\delta t$  is the half-period of the microwaves. For typical values of  $E = 100$  V/cm and  $\delta t = 50$  ps, we obtain  $\delta d = 17$  nm for electrons and 2 nm for holes. Therefore, in CdS regions with characteristic average dimensions of 15 nm  $\times$  5 nm, electrons will undergo frequent scattering with the CdS grain boundaries and they will be unable to move in phase with the microwave electric field. Thus, unless hopping between adjacent CdS nanocrystals occurs, electrons will hardly contribute to the microwave absorption signal. On the other hand, holes will experience the field as a perturbation of their diffusional motion, because their field-induced displacement is smaller than the size of the CdS domains. Hence, of the free carriers depicted in process III of Figure 1, only the hole is detectable by TRMC. Therefore, the end-of-pulse value of the  $\varphi \Sigma \mu$  product for the CdS/ZrO<sub>2</sub> sample in Figure 6b is attributed to the hole in CdS.

From Figure 6b, the product of the quantum yield times the mobility at the end of pulse at low light intensities is approximately  $3 \times 10^{-2} \text{ cm}^2/\text{V s}$ . Assuming the signal comes from holes with a mobility similar to that of the bulk, as discussed above, we can estimate the quantum yield for charge generation in the CdS domains at the end of (5 ns) pulse to be on the order of  $\varphi \sim 10^{-3}$ . Transient absorption studies have shown that the recombination/trapping lifetimes in ZrO<sub>2</sub>/CdS composites are  $\sim 80 \text{ ps}$ ,<sup>7</sup> which implies that significant excited-state relaxation occurs during the period of the TRMC instrument response function and that this rapid recombination and/or trapping severely limits  $\varphi$  in the nanosecond time domain. At high light intensities  $\varphi \Sigma \mu$  declines following an  $I_0^{-1/2}$  dependence, indicating a second-order recombination mechanism at high excitation levels.

We now discuss the difference in the  $\varphi \Sigma \mu$  product under 425 nm excitation for the TiO<sub>2</sub>/CdS and the ZrO<sub>2</sub>/CdS samples, as shown in Figure 6b. As discussed above, the photoconductance transient under 425 nm excitation is much longer-lived in the TiO<sub>2</sub>/CdS sample than in the ZrO<sub>2</sub>/CdS sample (Figure 4). It is interesting to note that the decay kinetics after 100 ns for the TiO<sub>2</sub>/CdS samples excited at 425 nm are almost identical to that of the bare TiO<sub>2</sub> sample. This suggests that the decay at long times is dominated by the intrinsic properties of TiO<sub>2</sub>. As mentioned above, TA studies demonstrate a short excited-state lifetime for CdS deposited on ZrO<sub>2</sub>, whereas rapid electron injection was observed from photoexcited CdS to TiO<sub>2</sub>, on the order of 10–50 ps.<sup>7</sup> These characteristic times play different roles in the signal we measure in the current experiments. In the case of ZrO<sub>2</sub>/CdS, the excited state only involves an electron–hole pair in CdS because there is no electron injection to the oxide. The lifetime of this excited state is shorter than the laser pulse and recombination/trapping of photogenerated carriers in CdS limits the quantum yield for charge carrier generation, consistent with the relatively small signal and instrument response limited decays observed in Figures 4 and 5. However, in the case of TiO<sub>2</sub>/CdS charge injection to TiO<sub>2</sub> is faster than recombination of the photogenerated carrier pair in CdS; therefore, the most probable outcome of photoexcitation of CdS is an electron in TiO<sub>2</sub> and a hole in CdS, as shown in process II of Figure 1. For this reason, the yield for free carrier generation is higher in this case, and as a consequence the end-of-pulse photoconductance values for the TiO<sub>2</sub>/CdS sample are higher than that for ZrO<sub>2</sub>/CdS by about a factor of 3. Finally, charge separation impedes recombination and the transients are longer-lived. As will be discussed below, the yield of free carrier generation in CdS/TiO<sub>2</sub> at early times is limited by hole trapping and not by recombination.

At low light intensities,  $\varphi \Sigma \mu$  for the TiO<sub>2</sub>/CdS sample under 425 nm excitation reaches a plateau of  $0.1 \text{ cm}^2/\text{V s}$ , which is higher than the reported electron mobility in TiO<sub>2</sub>.<sup>18</sup> This indicates that by the end of the pulse the signal for the TiO<sub>2</sub>/CdS sample under 425 nm excitation is dominated not by electrons in TiO<sub>2</sub> but by the highly mobile holes in CdS. Indeed, the light intensity dependence of the  $\varphi \Sigma \mu$  product for the CdS/ZrO<sub>2</sub> sample, which is dominated by holes in CdS as discussed above, exhibits the same plateau at low light intensities and decline at high light intensities. This observation of the carrier in the sensitizer dominating the signal is in contrast to previous work with organic sensitizers, in which the TRMC signals were attributed only to electrons in TiO<sub>2</sub>, due to the much lower carrier mobility in organic molecular sensitizers compared to inorganic semiconductors.<sup>13–21</sup>

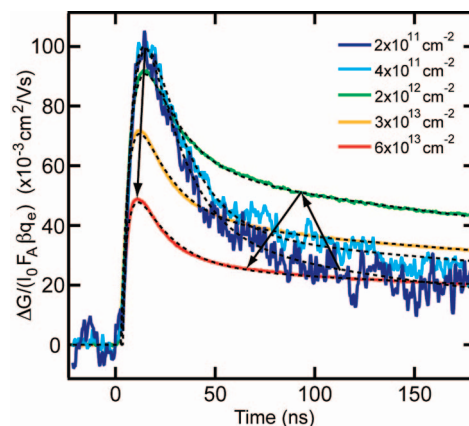


**Figure 8.** Representative absorbed-intensity-normalized photoconductance transients recorded for TiO<sub>2</sub>/CdS upon excitation at 425 nm using different light intensities, between  $2 \times 10^{11}$  and  $6 \times 10^{13} \text{ cm}^{-2}$ . Fits to the data using the model described in the text are illustrated with dotted lines. The arrows indicate the change of the photoconductance at different times as the light intensity increases (see text).

The contribution to the signal from different species becomes evident when looking at the intensity dependence of the decay kinetics, as depicted in Figure 8. The arrows indicate different regimes of the photoconductance transient, based on their light intensity dependence: while the end-of-pulse values increase with decreasing intensity until they reach a plateau (as shown in Figure 6b), the signal at longer times first increases and then decreases when lowering the excitation intensity, resembling the intensity dependence of the photoconductance signal for electrons in TiO<sub>2</sub> (Figure 6a). In contrast, the transients for the CdS/ZrO<sub>2</sub> sample under 425 nm excitation showed an increase toward a plateau at low light intensities across the entire time scale of the measurement.

The transients recorded at different light intensities for the CdS-sensitized TiO<sub>2</sub> sample could be satisfactorily fitted using two exponential decays with characteristic times  $\tau_1$  and  $\tau_2$ , convoluted with the instrument response function that was an exponential decay with the characteristic response time of the microwave cavity ( $\tau = 18 \text{ ns}$ ), as shown below:

$$\frac{\Delta G(t)}{I_0 F_A \beta q_e} = [\exp(-t/\tau)] [A_1 \exp(-t/\tau_1) + A_2 \exp(-t/\tau_2)] \quad (4)$$

The fits, also shown in Figure 8, consistently yielded a fast component on the order 3–5 ns and a longer-lived contribution in the range 200–600 ns. The amplitudes,  $A_1$  and  $A_2$ , of the exponential terms (with units of  $\text{cm}^2/\text{Vs}$ ) represent the contribution of each component to  $\varphi \Sigma \mu$ , and are shown in Figure 9 as a function of incident photon flux.

The lifetime and intensity dependence of the long-lived component resemble the signals obtained upon illumination at 300 nm, and can therefore be attributed to the electrons in TiO<sub>2</sub>. It is remarkable that the long-lived component shows the trap-filling regime at low excitation intensities. This is consistent with the multiple trapping processes that the electrons injected to TiO<sub>2</sub> from photoexcited sensitizers will undergo (shown by the vertical dotted arrows in process II of Figure 1). As discussed above, the presence of CdS on the surface of TiO<sub>2</sub> does not appear to passivate the electron traps.

The short-lived component, following our previous discussion, corresponds to the holes remaining in CdS following charge separation. Indeed, its light-intensity dependence closely re-



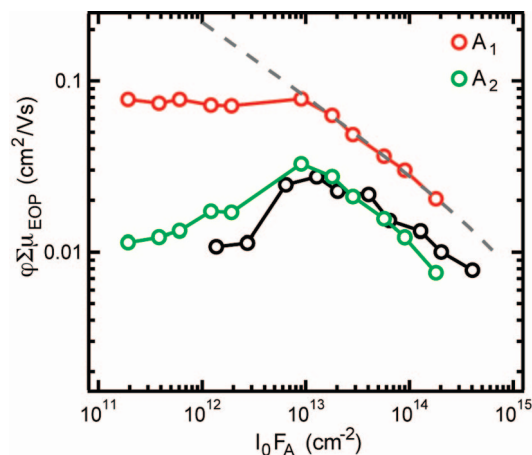


**Figure 9.** Contribution of the short (red circles) and long (green circles) components ( $A_1$  and  $A_2$  respectively) of the fitted signals to the end-of-pulse value of the photoconductance (see text). The black circles illustrate the intensity dependence for bare  $\text{TiO}_2$ , and the broken line is a fit of the high-intensity data to a power law, giving an exponent  $-0.43$ .

sembles that of CdS domains on  $\text{ZrO}_2$ , where the signal is dominated by the holes in CdS.

Note that the characteristic time of the short-lived component that results from the fit is shorter than the response time of the microwave cavity; therefore its value should not be taken to strictly represent an exact decay time. Our fitting process shows that this decay time (dominated by photocarriers in CdS) is faster than our measurement technique can resolve.

We can compare the  $\phi\sum\mu$  values obtained when illuminating at 300 nm and those obtained from the long-lived component of the 425 nm signal to estimate the number of electrons in  $\text{TiO}_2$  per photon absorbed in the CdS sensitizer,  $\phi$ . The values in both cases are very similar, implying that, upon excitation of the CdS sensitizer, electron injection into  $\text{TiO}_2$  is, per absorbed photon, as efficient as direct band gap excitation of the semiconductor, which is normally considered to be close to unity. This observation also suggests that the early-time decay in the transients of Figure 8 is due to hole trapping in CdS and not to recombination. Indeed, if recombination were the cause of the rapid decay, that would limit the density of photogenerated carriers in CdS and, consequently, the yield for electron injection to  $\text{TiO}_2$  per photon absorbed in the sensitizer.

In Figure 9,  $A_1$  decreases with laser intensity above  $9 \times 10^{12}$  absorbed photons following a power dependence close to an inverse square root, similar to the end-of-pulse values of Figure 6b, indicating that the yield for free carrier generation at high excitation intensities is limited by second-order processes. It should be noted that the transition from one regime to the other occurs at the same absorbed intensity for the two components of the CdS-sensitized  $\text{TiO}_2$  and also the bare oxide. Previous studies showed that the threshold for this change occurs when there is approximately one photon absorbed per  $\text{TiO}_2$  nanoparticle.<sup>18</sup> As our TEM images show, in this case, eight chemical bath reaction cycles results in an average size of the CdS domains corresponding to approximately one domain per  $\text{TiO}_2$  particle. Multiple excitations per CdS domain are expected to induce second-order effects and will contribute to the decline at high light intensities, as confirmed by our data.

As shown in Figure 7, the photoconductance values of the  $\text{TiO}_2/\text{CdS}$  sample closely follow the CdS absorption, indicating a constant yield for free carrier generation at all wavelengths. With regard to sensitization of  $\text{TiO}_2$  in a photovoltaic applica-

tion, the optimum number of deposition cycles for a working solar cell is a tradeoff between strong light-harvesting and efficient electron injection. Larger dots have a broader absorption of the solar spectrum, but their conduction band gets closer to that of the  $\text{TiO}_2$  reducing the driving force for electron injection and potentially inhibiting it. This effect is not apparent at the longest wavelengths used in the present study, and hence larger CdS crystals would be expected to yield more efficient solar cells. Further TRMC experiments, on samples where an increased number of SILAR cycles have been used to prepare the CdS domains, are in progress to elucidate when this effect appears and which is the minimum band offset for efficient charge separation.

## 5. Conclusions

We present a microwave conductivity study of charge injection following photoexcitation of CdS domains grown on nanoporous  $\text{TiO}_2$  and  $\text{ZrO}_2$  by a chemical bath deposition method. The data and analysis presented here extend previous studies on organic sensitizers, where the hole left in the sensitizer has low mobility and is not detectable, to a case of an inorganic sensitizer (CdS) where the hole that results from the charge separation process is mobile and contributes to the photoconductance. The CdS sensitizer extends the optical absorption of the films well into the visible range. Mobile charge carriers are generated with a low yield following photoexcitation of the CdS grown on  $\text{ZrO}_2$ ; there is no injection into the oxide and the short-lived photoconductance signal is attributed to the hole in CdS. In contrast, illumination of CdS domains grown on  $\text{TiO}_2$  results in very efficient charge generation and electron injection into the  $\text{TiO}_2$  nanoparticles, which produces a long-lived photoconductance signal due to physical separation of the carriers. In the  $\text{TiO}_2/\text{CdS}$  sample we can decouple the electron and hole contributions to the microwave photoconductance signal based on their different time scales and light-intensity dependence. This allows us to obtain the electron contribution to the photoconductance and compare it to the signal from direct band gap excitation of  $\text{TiO}_2$ . We conclude that the quantum yield for electron injection in  $\text{TiO}_2$  per photon absorbed by the sensitizer is as high as direct band gap excitation of the semiconductor itself, generally assumed to be close to unity. Charge carrier generation is limited by second-order processes as the incident intensity increases above one photon per CdS domain. We also show that the photoconductance action spectrum follows the absorption of the CdS domains, which indicates that the charge injection efficiency does not depend on wavelength in the range where the CdS absorbs (425–550 nm). Notably, the CdS domains do not seem to change the surface trapping of electrons in  $\text{TiO}_2$ , presumably due to incomplete coverage of the  $\text{TiO}_2$  surface.

**Acknowledgment.** The authors gratefully acknowledge Prof. Dr. L. D. A. Siebbeles and Dr. M. P. de Haas of the Delft University of Technology for useful discussions regarding TRMC measurements. We also thank Dr. Jao van de Lagemaat for useful discussions. J.P., A.J.F., J.L.B., G.R., and N.K. were funded by the Photochemistry and Radiation Research program of the U.S. Department of Energy, Office of Science, Basic Energy Sciences, Division of Chemical Sciences, Geosciences and Biosciences, under Contract No. DEAC36-99GO10337 to NREL. D.C.S. was supported by the Xcel Energy Renewable Development Fund.

## References and Notes

- (1) Gerischer, H.; L bke, M. *J. Electroanal. Chem.* **1986**, *204*, 225.
- (2) Vogel, R.; Pohl, K.; Weller, H. *Chem. Phys. Lett.* **1990**, *174*, 241.



- (3) Vogel, R.; Hoyer, P.; Weller, H. *J. Phys. Chem.* **1994**, *98*, 3183.
- (4) Peter, L. M.; Riley, D. J.; Tull, E. J.; Wijayantha, K. G. U. *Chem. Commun.* **2002**, 1030.
- (5) Niitsoo, O.; Sarkar, S. K.; Pejoux, C.; Rühle, S.; Cahen, D.; Hodes, G. *J. Photochem. Photobiol., A* **2006**, *181*, 306.
- (6) Chang, C.-H.; Lee, Y.-L. *Appl. Phys. Lett.* **2007**, *91*, 53503.
- (7) Blackburn, J. L.; Selmarten, D. C.; Nozik, A. J. *J. Phys. Chem. B* **2003**, *107*, 14154.
- (8) Robel, I.; Kuno, M.; Kamat, P. V. *J. Am. Chem. Soc.* **2007**, *129*, 4136.
- (9) Robel, I.; Subramanian, V.; Kuno, M.; Kamat, P. V. *J. Am. Chem. Soc.* **2006**, *128*, 2385.
- (10) Sant, P. A.; Kamat, P. V. *Phys. Chem. Chem. Phys.* **2002**, *4*, 198.
- (11) Trupke, T.; Würfel, P.; Uhlendorf, I. *J. Phys. Chem. B* **2000**, *104*, 11484.
- (12) de Haas, M. P.; Warman, J. M. *Chem. Phys.* **1982**, *73*, 35.
- (13) Huijser, A.; Savenije, T. J.; Kotlewski, A.; Picken, S. J.; Siebbeles, L. D. A. *Adv. Mater.* **2006**, *18*, 2234.
- (14) Huijser, A.; Savenije, T. J.; Siebbeles, L. D. A. *Thin Solid Films* **2006**, *511*, 208.
- (15) Kroeze, J. E.; Savenije, T. J.; Warman, J. M. *C. R. Chim.* **2006**, *9*, 667.
- (16) Huijser, A.; Savenije, T. J.; Kroeze, J. E.; Siebbeles, L. D. A. *J. Phys. Chem. B* **2005**, *109*, 20166.
- (17) Kroeze, J. E.; Koehorst, R. B. M.; Savenije, T. J. *Adv. Funct. Mater.* **2004**, *14*, 992.
- (18) Kroeze, J. E.; Savenije, T. J.; Warman, J. M. *J. Am. Chem. Soc.* **2004**, *126*, 7608.
- (19) Kroeze, J. E.; Savenije, T. J. *Thin Solid Films* **2004**, *451–52*, 54.
- (20) Kroeze, J. E.; Savenije, T. J.; Vermeulen, M. J. W.; Warman, J. M. *J. Phys. Chem. B* **2003**, *107*, 7696.
- (21) Savenije, T. J.; Vermeulen, M. J. W.; de Haas, M. P.; Warman, J. M. *Sol. Energy Mater. Sol. Cells* **2000**, *61*, 9.
- (22) Bak, T.; Nowotny, J.; Nowotny, M. K. *J. Phys. Chem. B* **2006**, *110*, 21560.
- (23) Wegewijs, B. R.; Dicker, G.; Piris, J.; Garcia, A. A.; de Haas, M. P.; Warman, J. M. *Chem. Phys. Lett.* **2000**, *332*, 79.
- (24) Savenije, T. J.; de Haas, M. P.; Warman, J. M. *Z. Phys. Chem.* **1999**, *212*, 201.
- (25) Zhu, K.; Kopidakis, N.; Neale, N. R.; van de Lagemaat, J.; Frank, A. J. *J. Phys. Chem. B* **2006**, *110*, 25174.
- (26) Kopidakis, N.; Neale, N. R.; Zhu, K.; van de Lagemaat, J.; Frank, A. J. *Appl. Phys. Lett.* **2005**, *87*, 202106.
- (27) van de Lagemaat, J.; Park, N.-G.; Frank, A. J. *J. Phys. Chem. B* **2000**, *104*, 2044.
- (28) Kopidakis, N.; Schiff, E. A.; Park, N.-G.; van de Lagemaat, J.; Frank, A. J. *J. Phys. Chem. B* **2000**, *104*, 3930.
- (29) Schlichthörl, G.; Park, N.-G.; Frank, A. J. *J. Phys. Chem. B* **1999**, *103*, 782.
- (30) de Jongh, P. E.; Vanmaekelbergh, D. *J. Phys. Chem. B* **1997**, *101*, 2716.
- (31) Dloczik, L.; Ieperuma, O.; Lauermann, I.; Peter, L. M.; Ponomarev, E. A.; Redmond, G.; Shaw, N. J.; Uhlendorf, I. *J. Phys. Chem. B* **1997**, *101*, 10281.
- (32) Sze, S. M.; Ng, K. K. *Physics of semiconductor devices*; Wiley: Hoboken, NJ, 2007.

JP800527R